

Agent-Based Optimal Control for Image Processing

Alessio Oliviero^{*1}, Simone Cacace^{†1}, and Giuseppe Visconti^{‡1}

¹Department of Mathematics, Sapienza University of Rome, Rome, Italy

October 21, 2025

Abstract

We investigate the use of multi-agent systems to solve classical image processing tasks, such as colour quantization and segmentation. We frame the task as an optimal control problem, where the objective is to steer the multi-agent dynamics to obtain colour clusters that segment the image. To do so, we balance the total variation of the colour field and fidelity to the original image. The solution is obtained resorting to primal-dual splitting and the method of multipliers. Numerical experiments, implemented in parallel with CUDA, demonstrate the efficacy of the approach and its potential for high-dimensional data.

Keywords. Multi-agent systems; Image processing; Unsupervised learning; Augmented Lagrangian; Primal-dual splitting; Method of multipliers; CUDA implementation.

MSC2020. 68U10 (Image processing); 82C22 (Interacting particle systems (statistical mechanics / agent-based modeling)); 49M25 (Discrete approximations in optimal control); 49N90 (Applications of optimal control and differential games).

1 Introduction

Image segmentation and colour quantization [10, 31] are fundamental tasks in image processing, computer vision, and pattern recognition. Their goal is to simplify the visual representation of an image while preserving its essential structure and perceptual content. In segmentation, the objective is to divide the image domain into homogeneous regions according to some similarity criterion, typically based on intensity, texture, or spatial continuity. Colour quantization, on the other hand, aims at reducing the number of distinct colours or intensity levels in an image, providing a compact representation that is still visually coherent with the original.

Classical approaches to these problems include clustering-based methods such as the k -means [30], hierarchical clustering [2], and evolutionary or meta-heuristic techniques such as genetic algorithms [18]. While these methods have proven effective in many practical applications, they typically require the number of clusters or segments to be fixed a priori, which may not be known in advance and often depends on the specific image content. Moreover, their performance can be sensitive to initialization, noise, and outliers, limiting their robustness and their ability to adapt dynamically to different image structures. These approaches belong to the class of *unsupervised learning* techniques, which aim to discover the intrinsic organization of the data without relying on annotated training sets [25, 34].

^{*}alessio.oliviero@uniroma1.it

[†]simone.cacace@uniroma1.it

[‡]giuseppe.visconti@uniroma1.it

On the other hand, *supervised learning* methods have gained increasing attention in recent years, particularly through the use of deep and shallow neural networks [9, 21, 23, 28]. These models learn, from a sufficiently large and representative set of labelled examples, a non-linear mapping between input features and the corresponding segmentation masks. Well-trained networks can achieve high segmentation accuracy even for complex and heterogeneous images, benefiting from their expressive power and capacity for generalization. However, the effectiveness of these methods strongly depends on the quality and quantity of the available training data, as well as on the adopted training strategy. Supervised neural models therefore require extensive computational resources and carefully curated datasets to avoid bias and overfitting, which often limits their applicability in domains where labelled data are scarce or costly to obtain.

In recent years, there has been growing interest in alternative frameworks based on multi-agent systems [1, 17, 26], that describe the evolution of data distributions through collective or agent-based dynamics. Such approaches, inspired by models of self-organization in biology [13] and society [19], interpret clustering and denoising as emergent phenomena arising from local interactions among simple agents. This dynamical viewpoint offers a flexible and adaptive perspective on image processing, where segmentation and quantization can emerge naturally from the underlying interaction rules rather than being imposed externally.

In agent-based models, each datum – here, each pixel or colour intensity – is interpreted as an agent whose state evolves dynamically through interactions with its neighbours. The collective behaviour of the system then gives rise to emergent structures that naturally correspond to clusters or coherent regions. The main advantage of these dynamical approaches lies in their ability to adapt to the geometry of the data. Interactions can be defined not only in terms of feature similarity – such as the difference in intensity or colour – but also in terms of spatial proximity within the image domain. This allows for a natural coupling between the photometric and geometric components of the image, yielding models that are both data-driven and spatially coherent. Moreover, since the evolution of each agent is governed by continuous dynamics, these models are intrinsically well suited to incorporate regularization effects and to balance fidelity and smoothness through the tuning of the interaction parameters.

Particularly relevant examples in this context are the approaches based on the Kuramoto model for coupled oscillators [22], on the Hegselmann-Krause consensus dynamics [5, 20], and the mean-shift algorithm [12]. In all these examples, which can be classified as unsupervised learning methods, global consensus or partial clustering emerges spontaneously from local interaction rules, without the need to specify the number of clusters or groups a priori.

In this paper, we consider an image as a discrete set of agents located on a two-dimensional spatial domain. Each pixel is represented by a position $(x_i, y_i) \in \Omega \subset \mathbb{R}^2$ and an associated intensity or colour value $c_i \in [0, 1]$ (in the case of grey-scale images). The state of the system at a given time t is therefore described by the collection $\{(x_i, y_i, c_i(t))\}_{i=1}^N$, where N denotes the total number of pixels or agents. The temporal variable t does not correspond to physical time, but rather to an artificial evolution parameter that drives the system toward a segmented or quantized configuration.

The interaction between agents is designed to model both photometric similarity and spatial proximity. In particular, each agent tends to align its state c_i with the states of nearby agents whose intensities are similar, while the strength of this influence decays with spatial distance. This behaviour can be encoded by an interaction kernel which quantifies the attraction between two agents as a function of both their spatial and tonal distances.

Such a formulation provides a unified view of several well-known phenomena. If the interactions depend only on the difference in intensities, the dynamics resemble an alignment or consensus model on the colour space. If spatial proximity is also taken into account, one obtains a coupled model that promotes local regularity while preserving discontinuities at object boundaries. In this framework, image segmentation and colour quantization correspond to the

emergence of clusters in the intensity space, induced by the self-organization of the interacting agents.

The challenge, however, lies in determining how strongly the agents should interact at each time and at each spatial scale. Fixed interaction parameters may lead either to excessive smoothing – erasing fine details – or to poor denoising and fragmentation. To overcome this limitation, we introduce an optimal control approach, in which the interaction parameters are not fixed but evolve in time according to a control law designed to balance fidelity to the original image and regularization effects.

In previous models [5, 20], the agents represent the pixels of the image and are allowed to move within the spatial domain, while their associated colour or intensity values remain fixed. At the end of the evolution, the final colour assigned to each region is obtained by averaging the intensities of the pixels that have converged to the same spatial cluster. In other words, clustering occurs in the spatial domain, and the chromatic information is only used a posteriori to label the resulting groups.

In contrast, in the present work the positions of the agents are fixed, and the dynamics take place in the space of intensity values. Each agent (i.e., pixel) interacts with its neighbours according to both tonal and spatial similarity, but its colour value $c_i(t)$ evolves in time as a consequence of these interactions. Spatial proximity thus serves only to define the neighbourhood relations and interaction strengths, while the actual evolution occurs in the intensity space. This shift of perspective allows for a more direct coupling between local photometric features and their global organization, yielding a smoother and more adaptive quantization process.

Another important difference with respect to previous studies lies in the choice of the interaction parameters. In earlier models, these parameters were typically fixed at the initial time, or selected through exhaustive search procedures based on external optimization criteria. Such strategies are computationally expensive and prevent the model from adapting dynamically to the evolving structure of the image. Here, instead, the interaction coefficients are treated as time-dependent control variables, whose evolution is determined by an optimal control problem designed to minimize a suitable cost functional. This formulation enables an automatic, adaptive regulation of the interaction strength, balancing fidelity to the original image and smoothness of the reconstructed one.

Since we are interested only in the final state of the system, that is the final quantized image, the optimisation task is formulated as a Mayer-type problem. We first investigate a cost functional involving a quadratic penalty on the colour gradient and derive an optimality system, which we solve numerically using a standard direct-adjoint looping (DAL) algorithm. While effective in some scenarios, this approach reveals limitations related to edge preservation. To overcome this, we then introduce a more robust model based on total variation (TV) minimization, a standard in modern image processing for its edge-preserving properties [8, 29]. The non-smooth nature of the TV functional necessitates a more advanced primal-dual formulation, which we solve as a saddle-point problem via the Alternating Direction Method of Multipliers (ADMM) [4].

The entire numerical scheme is implemented in a parallel computing architecture using CUDA to handle the high dimensionality inherent in image data. This parallelization is naturally suited to our model, as the evolution of each pixel can be computed for each time step simultaneously across all pixels. Consequently, the synchronization of the device is necessary only once per time step, making the approach highly efficient. Our results demonstrate that this optimal control framework, particularly with the total variation cost, provides a flexible and effective method for colour quantization and image segmentation, successfully navigating the trade-off between clustering and feature preservation.

The rest of this paper is organized as follows. In Section 2, we introduce the multi-agent system, detailing the differential equations that govern the evolution of the image and defining the space of admissible control functions. Section 3 is dedicated to the first optimal control

formulation. We define a cost functional based on the L^2 norm of the intensity gradient, establish the well-posedness of the problem, and derive the corresponding optimality system. We then present the direct-adjoint looping (DAL) algorithm used for its numerical approximation and discuss the results of numerical tests, highlighting both the strengths and weaknesses of this approach. To address these limitations, in Section 4 we introduce an improved model based on total variation minimisation. We reformulate the problem as a saddle-point problem for a regularised functional and detail the Alternating Direction Method of Multipliers (ADMM) used to solve it. This section concludes with a series of numerical experiments comparing the performance of the two proposed algorithms, demonstrating the superiority of the total variation approach in preserving sharp edges. Finally, Section 5 provides concluding remarks, summarising our contributions and suggesting possible future lines of research.

2 Mathematical model

Let I be a grey-scale image composed of N pixels. We represent it as a rectangular matrix, whose entries contain the pixels' colour intensity normalised in $[0, 1]$. To keep consistency with Cartesian coordinates, the rows of the matrix are ordered from bottom to top. We associate to each pixel an agent

$$p_i = [x_i, y_i, c_i]^\top, \quad i = 1, \dots, N,$$

where (x_i, y_i) are the (discrete) spatial coordinates of the pixel and c_i is its grey-level value. Hence, $p_1 = [x_1, y_1, c_1]$ corresponds to the bottom-left pixel of I and $p_N = [x_N, y_N, c_N]$ to the top-right one.

The key idea is to keep the position of the agents fixed, thereby preserving the spatial correlation among them, and let the colour component evolve over a finite time horizon $[0, T]$ according to a system of coupled ordinary differential equations, which, for each $i = 1, \dots, N$, reads

$$\begin{cases} \dot{c}_i(t) = \frac{1}{N} \sum_{j=1}^N \phi(r_{ij}^\varepsilon(t)) (c_j(t) - c_i(t)), & t \in (0, T], \\ c_i(0) = c_i^0. \end{cases} \quad (1)$$

Here $\phi : \mathbb{R} \rightarrow \mathbb{R}$ is a differentiable interaction kernel that weighs the influence of neighbouring agents, and the quantity

$$r_{ij}^\varepsilon(t) = \frac{\varepsilon_x(t)}{2} [(x_j - x_i)^2 + (y_j - y_i)^2] + \frac{\varepsilon_c(t)}{2} (c_j(t) - c_i(t))^2 \quad (2)$$

measures a distance between p_i and p_j in the extended space $\Omega \times [0, 1]$. The time-dependent parameters $\varepsilon_x(\cdot)$ and $\varepsilon_c(\cdot)$ play the role of anisotropic scaling factors, respectively quantifying the relevance of spatial separation and colour disparity in the interaction. When ε_x is large compared with ε_c , agents tend to interact mostly with spatial neighbours, leading to diffusion-like smoothing; conversely, a small ε_x enhances long-range connections based on colour similarity.

For any fixed $t \geq 0$, the set of p_j that effectively influence p_i is determined by the support of ϕ applied to $r_{ij}^\varepsilon(t)$. When ϕ has compact support, the interaction domain is a bounded ellipsoid in $[0, 1]^3$, centred at p_i and with semi-axes proportional to $(\varepsilon_x(t)^{-1/2}, \varepsilon_x(t)^{-1/2}, \varepsilon_c(t)^{-1/2})$. The time-dependence of $(\varepsilon_x, \varepsilon_c)$ allows the size of this ellipsoid to adapt, letting agents that were initially disconnected become linked during the evolution, or vice versa. Their evolution can be either fixed, scheduled, or determined through an optimal control strategy, as presented in the following section. Clearly, not every choice of $\varepsilon := (\varepsilon_x, \varepsilon_c)$ is suitable for our model. For example, negative values would have no physical meaning in this context.

Definition 2.1. Let E be a convex, compact subset of $[0, +\infty) \times [0, +\infty)$. We define the space of *admissible controls*

$$\mathcal{E} := \{\varepsilon : \mathbb{R}_0^+ \rightarrow E \text{ measurable}\}. \quad (3)$$

Classical results for opinion dynamics models [26] ensure that, under mild assumptions on ϕ , the solution converges to a finite number of clusters in finite time. These clusters correspond to distinct regions of Ω over which the grey intensity is constant: a colour quantization of the original image.

3 The optimal control problem

In this section, we formulate a control problem with the goal of obtaining an optimal quantization of the input image I . For analytical convenience, we assume that the image is continuous in both space and intensity, and we rescale it so that $(x_i, y_i) \in \Omega := [0, 1]^2$ for all pixels. We adopt the notation $c(x, t)$ to refer to the continuous version of the colour field at point $x \in \Omega$ and time $t \in [0, T]$.

The first step is to define a cost functional that penalises colour variation, while at the same time keeping memory of the original image.

Definition 3.1. Let $\alpha > 0$. We define the cost functional $J : H^1(\Omega) \rightarrow \mathbb{R}$ as

$$J(u) = \int_{\Omega} \frac{1}{2} |\nabla u(x)|^2 + \frac{\alpha}{2} (u(x) - I(x))^2 \, dx. \quad (4)$$

When applied to an image $c(\cdot, t)$ at a fixed time t , the first term in (4) measures fluctuations in the colour field, while the second one enforces fidelity to the original picture I . In this case, J is implicitly dependent on $\varepsilon = (\varepsilon_x, \varepsilon_c)$, as these parameters are what determines the evolution of the image from the initial condition I to $c(\cdot, t)$. In this light, the cost functional can also be seen as the cost associated with the *control policy* $\varepsilon \in \mathcal{E}$ over the time interval $[0, t]$. With a slight abuse of notation, in Algorithm 1 we will refer to this control-to-cost map as $J(\varepsilon)$. The weight α balances the two cost components and is assumed to be a given parameter of the problem. We remark that the choice of this functional is motivated by the fact that the two terms in J produce opposite behaviours: for $\alpha = 0$ the minimiser is just a constant (single colour) image, whereas for $\alpha \rightarrow +\infty$ the minimizer will result in the original image I . Since the multi-agent dynamics is ultimately driven by the control policy ε , affecting spatial and colour interactions, these extremal configurations correspond respectively to full (one to all) and zero interactions, leading on the one hand to colour consensus, on the other hand to a clusterisation in which each pixel is itself a single cluster. Hence, by tuning α , we expect to indirectly adjust the number of clusters in the final image. This may appear to be analogous to choosing a priori a fixed number of clusters in classical algorithms like k -means, but there is a fundamental difference between the two approaches. Selecting the number of segments is a *prescriptive* constraint, while α is a *descriptive* parameter. With classical methods, the user imposes a structure on the data and this is a strong assumption that may not be supported by the data itself. With our model, instead, the number of clusters is an emergent property. This is a data-driven result, not a predefined guess.

The following result ensures the well-posedness of the problem

Theorem 3.1. Let $\alpha > 0$. Then the functional $J : H^1(\Omega) \rightarrow \mathbb{R}$ in Definition 3.1 has a unique global minimum.

Proof. It is immediate to verify that J is weakly lower semi-continuous and bounded from below, as it is always non negative. Moreover,

$$J(u) = \frac{1}{2} \|\nabla u\|_{L^2(\Omega)}^2 + \frac{\alpha}{2} \|u\|_{L^2(\Omega)}^2 - \alpha \langle u, I \rangle_{L^2(\Omega)} + \frac{\alpha}{2} \|I\|_{L^2(\Omega)}^2$$

and, by applying Cauchy–Schwartz and Young inequalities, there exist $C, D > 0$ such that

$$J(u) \geq C \|u\|_{H^1(\Omega)}^2 - D,$$

implying coercivity of J . By the Direct Method in the calculus of variations, J admits a minimum.

To ensure uniqueness, we observe that the functional is twice Fréchet differentiable and its second variation reads

$$J''(u)[v, w] = \int_{\Omega} \nabla v \cdot \nabla w + \alpha v w \, dx,$$

therefore, since $\alpha > 0$, the quadratic form $J''(u)[v, v]$ is positive definite for any direction v . Hence, J is strictly convex and this proves the thesis. \square

Since we are interested in optimising the final configuration of the multi-agent system (1), we formulate the following Mayer problem:

$$\underset{\varepsilon \in \mathcal{E}}{\text{minimise}} \quad J(c(\cdot, T; \varepsilon)) \quad \text{subject to (1)-(2).} \quad (5)$$

A minimiser $\varepsilon^* \in \mathcal{E}$ of J is called an *optimal control* and the evolution of the multi-agent system associated with it is the optimal trajectory.

Remark 1 (On the choice of T and E). Although the optimal control problem can be stated for general $T \in (0, +\infty)$ and $E \subset\subset [0, +\infty) \times [0, +\infty)$, from a practical point of view not every choice is equivalent. One should ensure that the compact set E is large enough to allow both global interactions, i.e. $\phi(r_{ij}^\varepsilon) > 0$ for any $i, j = 1, \dots, N$, and no interactions at all, i.e. $\phi(r_{ij}^\varepsilon) = 0$ for all $i, j = 1, \dots, N$. Moreover, T should be large enough to enable the formation of clusters – or, in the language of opinion dynamics, to let the agents reach consensus. At the same time, an excessively far time horizon would just add a computational burden in the numerical simulations without yielding any benefit.

3.1 Numerical approximation

Given the complexity and high-dimensionality of the system, solving (5) analytically is unfeasible. Therefore, we resort to a numerical approximation scheme following the variational (or direct) approach. To keep the notation simple, from this point onwards, we will write $F(c(x, t), \varepsilon(t))$ to refer to the space-continuous version of the right-hand side of (1).

We introduce the adjoint state function $\lambda : \Omega \times (0, +\infty) \rightarrow \mathbb{R}$ and use it as a Lagrange multiplier to encode the dynamical constraints (1)-(2) into the augmented cost functional

$$\tilde{J}(c, \lambda, \varepsilon) = \int_0^T \int_{\Omega} \lambda(x, t) \cdot [\partial_t c(x, t) - F(c(x, t), \varepsilon(t))] \, dx \, dt + J(c(\cdot, T; \varepsilon)). \quad (6)$$

In this way, assuming for the moment unbounded controls, by imposing $\delta \tilde{J} = 0$ we can formally derive the optimality system

$$\partial_t c(x, t) = F(c(x, t), \varepsilon(t)), \quad c(x, 0) = I(x), \quad (7a)$$

$$\partial_t \lambda(x, t) = -\partial_c F(c(x, t), \varepsilon(t)) \cdot \lambda(x, t), \quad \lambda(x, T) = -\Delta c(x, T) + \alpha(c(x, T) - I(x)), \quad (7b)$$

$$\int_{\Omega} \partial_{\varepsilon} F(c(x, t), \varepsilon(t)) \cdot \lambda(x, t) \, dx = 0, \quad (7c)$$

for a.e. $x \in \Omega$ and $t \in (0, T)$. The complete derivation can be found in Appendix A. System (7) can be approximated with a simple direct-adjoint looping (DAL) algorithm, which is essentially a steepest descent along the functional J . For our purposes, we add a projection Π_E onto the convex set E to bound the control at each step. Moreover, we employ a two-way Armijo backtracking line search method [3] to select the best descent step-size at each iteration, resulting in Algorithm 1. Due to the non-linearity of the ODE system (1), the control-to-state map $\varepsilon \mapsto c(\cdot, T; \varepsilon)$ is not convex. As a consequence, we can only expect convergence to a local minimiser.

Algorithm 1 DAL algorithm for system (7) with two-way Armijo backtracking line search

Require: Initial guess for the control $\varepsilon^{(0)}, \sigma^{(0)} > 0, b, c \in (0, 1)$

- 1: $j \leftarrow 0$
- 2: **repeat**
- 3: Integrate (7a) forward in time to obtain $c^{(j)}$
- 4: Using $c^{(j)}$ for the terminal condition, integrate (7b) backward in time to get $\lambda^{(j)}$
- 5: $D^{(j)} \leftarrow \partial_\varepsilon F(c^{(j)}, \varepsilon^{(j)}) \cdot \lambda^{(j)}$
- 6: $k \leftarrow 0, \tau^{(0)} \leftarrow \sigma^{(j)}$
- 7: **if** $J(\Pi_E(\varepsilon^{(j)} - \sigma^{(j)} D^{(j)})) > J(\varepsilon^{(j)}) - c \sigma^{(j)} |D^{(j)}|^2$ **then**
- 8: **while** $J(\Pi_E(\varepsilon^{(j)} - \tau^{(k)} D^{(j)})) > J(\varepsilon^{(j)}) - c \tau^{(k)} |D^{(j)}|^2$ **do**
- 9: $\tau^{(k+1)} \leftarrow b \tau^{(k)}$
- 10: $k \leftarrow k + 1$
- 11: **end while**
- 12: **else**
- 13: **while** $J(\Pi_E(\varepsilon^{(j)} - \tau^{(k)} D^{(j)})) \leq J(\varepsilon^{(j)}) - c \tau^{(k)} |D^{(j)}|^2$ **do**
- 14: $\tau^{(k+1)} \leftarrow \tau^{(k)}/b$
- 15: $k \leftarrow k + 1$
- 16: **end while**
- 17: **end if**
- 18: $\sigma^{(j+1)} \leftarrow \tau^{(k)}$
- 19: $\varepsilon^{(j+1)} \leftarrow \Pi_E(\varepsilon^{(j)} + \sigma^{(j+1)} D^{(j)})$
- 20: $j \leftarrow j + 1$
- 21: **until** convergence

Remark 2 (Convergence criteria for the DAL algorithm). When the control is unconstrained, the typical convergence criterion to verify is

$$\partial_\varepsilon F(c^{(k)}, \varepsilon^{(k)}) \cdot \lambda^{(k)} < \eta$$

for some fixed tolerance $0 < \eta \ll 1$, since a necessary condition for optimality is that the quantity above equals zero [27]. However, when the control is constrained, the equality is not verified on the boundary of the compact set E . In this case, one should check the variational inequalities

$$\partial_\varepsilon F(c^{(k)}, \varepsilon^{(k)}) \cdot \lambda^{(k)} \geq 0 \quad \text{and} \quad \partial_\varepsilon F(c^{(k)}, \varepsilon^{(k)}) \cdot \lambda^{(k)} \leq 0$$

component-wise and point-wise in time (for a.e. $t \in (0, T)$ in the continuous version), respectively on the lower and upper active contact sets $\{\varepsilon_i = \varepsilon_i^{\min}\}$ and $\{\varepsilon_i = \varepsilon_i^{\max}\}$, for $i = x, c$ (see [32] for further details).

Alternatively, the criterion based on the vanishing gradient can be substituted with stationarity of the cost functional

$$\frac{|J(\varepsilon^{(j)}) - J(\varepsilon^{(j-1)})|}{J(\varepsilon^{(j-1)})} < \eta.$$

In case of non-convex functionals, second order necessary optimality conditions may also be checked to make sure the descent has not stopped on a plateau. We refer to [6, 11] for further details about these conditions and their application, which we will not utilise in this work.

3.2 Numerical tests

In this section, we present numerical simulations obtained by applying Algorithm 1. For all experiments, we set $T = 125$ and discretise the time interval $[0, T] = [0, 125]$ with a uniform step size $\Delta t = 0.25$. The spatial discretisation is naturally determined by the pixel structure

of the image, on which we impose Neumann boundary conditions. In particular, for each $i = 1, \dots, N$, we have

$$\frac{\partial F_i}{\partial c_k} = \begin{cases} \frac{1}{N} [\varphi'(r_{ik}^\varepsilon) \varepsilon_c (c_k - c_i)^2 + \varphi(r_{ik}^\varepsilon)] & \text{if } k \neq i \\ -\frac{1}{N} \sum_{j=1}^N [\varphi'(r_{ij}^\varepsilon) \varepsilon_c (c_j - c_i)^2 + \varphi(r_{ij}^\varepsilon)] & \text{if } k = i \end{cases} \quad (8)$$

$$\frac{\partial F_i}{\partial \varepsilon_x} = \frac{1}{2N} \sum_{j=1}^N \varphi'(r_{ij}^\varepsilon) ((x_j - x_i)^2 + (y_j - y_i)^2) (c_j - c_i) \quad (9)$$

$$\frac{\partial F_i}{\partial \varepsilon_c} = \frac{1}{2N} \sum_{j=1}^N \varphi'(r_{ij}^\varepsilon) (c_j - c_i)^3 \quad (10)$$

where the compactly supported interaction kernel is given by the C^2 Wendland function [33]

$$\varphi(r) := \begin{cases} (4r - 1)(1 - r)^4, & 0 \leq r \leq 1, \\ 0, & \text{otherwise.} \end{cases} \quad (11)$$

This kind of interaction kernels are standard in the smoothed particle hydrodynamics (SPH) literature, as they bring numerous advantages over gaussian or spline functions [14]. They are less subject to numerical noise and reduce the formation of artefacts. Moreover, being piecewise polynomial, they are computationally cheap – whereas exponential functions can impact performance – and their derivatives are explicit, still piecewise polynomial, and numerically stable.

The discrete Laplacian in (7b) is approximated using standard second-order centred finite differences, and time integration is performed with an explicit Euler scheme. In accordance with Remark 1, we set $E = [2, 1100]^2$ and initialise the control as $\varepsilon_x^{(0)} = \varepsilon_c^{(0)} \equiv 57$ at all discrete times. For the two-way Armijo line search, we choose $\sigma^{(0)} = 1$, $b = \frac{1}{2}$, and $c = 10^{-4}$. Convergence is assessed via the stationarity of the cost functional – computed with a rectangular quadrature rule – with tolerance $\eta = 10^{-10}$ (see Remark 2).

The routine is implemented in CUDA C and executed on an NVIDIA H100 NVL GPU, hosted on the *Lagrange* server of the Department of Mathematics, Sapienza University of Rome. In this way, the computations are parallelised over the pixels, yielding a significant performance improvement.

For the first experiment, we consider the image shown in the left panel of Figure 1, which depicts a magnetic resonance image (MRI) of a brain tumour [24, Figure 1B]. The colour distribution of the pixels is displayed in the right panel of the same figure. The output of Algorithm 1 for three different values of the fidelity parameter $\alpha > 0$ is reported in Figure 2. As expected, α has a decisive influence on the optimisation outcome. For large values of α , the reconstruction closely follows the original image, and three distinct clusters emerge, corresponding to the background, healthy brain tissue, and tumour. For intermediate values, we observe a distinctive blurring effect caused by the penalisation of colour variation; consequently, edges are not well preserved. For smaller values of α , the gradient term dominates, and global interactions drive the agents to consensus, producing a single cluster that represents the average colour of the image.

For a second experiment, we repeat the procedure on a more complex picture, shown in Figure 3. The pixel distribution in the right panel reveals the absence of both purely black and purely white values. This makes the clustering task more challenging, as most agents are already concentrated within a narrow range of colour coordinates, despite representing different objects in the image. Figure 4 illustrates the results: for large α , the background wall and the floor are successfully flattened, but the bowl and the dog remain overly detailed. Reducing α improves

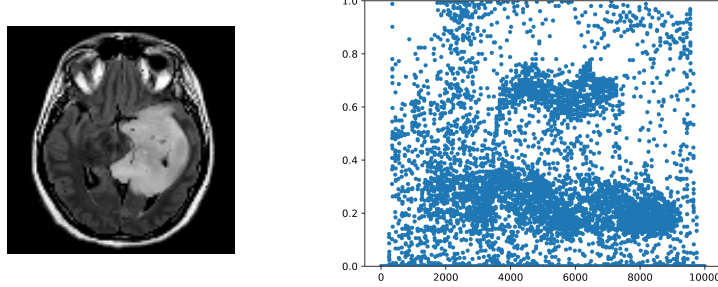


Figure 1: Magnetic resonance image of a brain tumour, from [24, Figure 1B]. On the left side, the original picture; on the right, colour value $c_i \in [0, 1]$ for every pixel p_i , $i = 1, \dots, N$.

the homogenisation of the bowl, but at the expense of blending the dog with the background. We therefore conclude that Algorithm 1 is only effective for images with high contrast between structural elements, such as those arising in medical imaging, but less suited to natural images with smoother colour variations.

4 Total variation minimisation

Based on the previous tests, we introduce a different cost functional, with the aim of preserving sharp edges and mitigating the diffusion effect. To this end, we consider the functional from the Rudin–Osher–Fatemi (ROF) model [29], given by

$$K(u) = \int_{\Omega} |\nabla u(x)| + \frac{\alpha}{2}(u(x) - I(x))^2 \, dx. \quad (12)$$

In practice, we replace the quadratic term $\frac{1}{2}|\nabla u|^2$ in 4 with the total variation of u . Despite this change, various results in the literature prove existence and uniqueness of a minimiser for (12), see for instance [7]. However, K is not Fréchet differentiable, and this prevents the use of gradient-based numerical methods. To circumvent this difficulty, we resort to a primal–dual regularisation of the problem.

Definition 4.1. Let $v \in L^2(\Omega; \mathbb{R}^2)$ be an auxiliary vector field, $\mu \in L^2(\Omega; \mathbb{R}^2)$ the corresponding multiplier, and $\alpha, \rho > 0$. We define the regularised cost functional $L : H^1(\Omega) \times L^2(\Omega; \mathbb{R}^2) \times L^2(\Omega; \mathbb{R}^2) \rightarrow \mathbb{R}$ as

$$L(u, v, \mu) = \int_{\Omega} |v(x)| + \mu(x) \cdot (v(x) - \nabla u(x)) + \frac{\rho}{2}|v(x) - \nabla u(x)|^2 + \frac{\alpha}{2}(u(x) - I(x))^2 \, dx. \quad (13)$$

In this way, we move from a minimum problem for K to a saddle point problem for L , which is smooth.

Theorem 4.1. *There exists a saddle point for the functional $L : H^1(\Omega) \times L^2(\Omega; \mathbb{R}^2) \times L^2(\Omega; \mathbb{R}^2) \rightarrow \mathbb{R}$ defined in (13). In particular, the strong duality condition holds:*

$$\min_{u \in H^1(\Omega), v \in L^2(\Omega; \mathbb{R}^2)} \max_{\mu \in L^2(\Omega; \mathbb{R}^2)} L(u, v, \mu) = \max_{\mu \in L^2(\Omega; \mathbb{R}^2)} \min_{u \in H^1(\Omega), v \in L^2(\Omega; \mathbb{R}^2)} L(u, v, \mu). \quad (14)$$

Proof. We observe that the functional is weakly lower semi-continuous with respect to u and v , and weakly continuous w.r.t. μ . Moreover, L is strictly convex in the primal variables and concave in the dual one. As a matter of fact, since $\alpha, \rho > 0$,

- $u \mapsto \int_{\Omega} \frac{\rho}{2}|v - \nabla u|^2 - \mu \nabla u + \frac{\alpha}{2}(u - I)^2$ is strictly convex,
- $v \mapsto \int_{\Omega} \frac{\rho}{2}|v - \nabla u|^2 + |v| + \mu v$ is strictly convex,

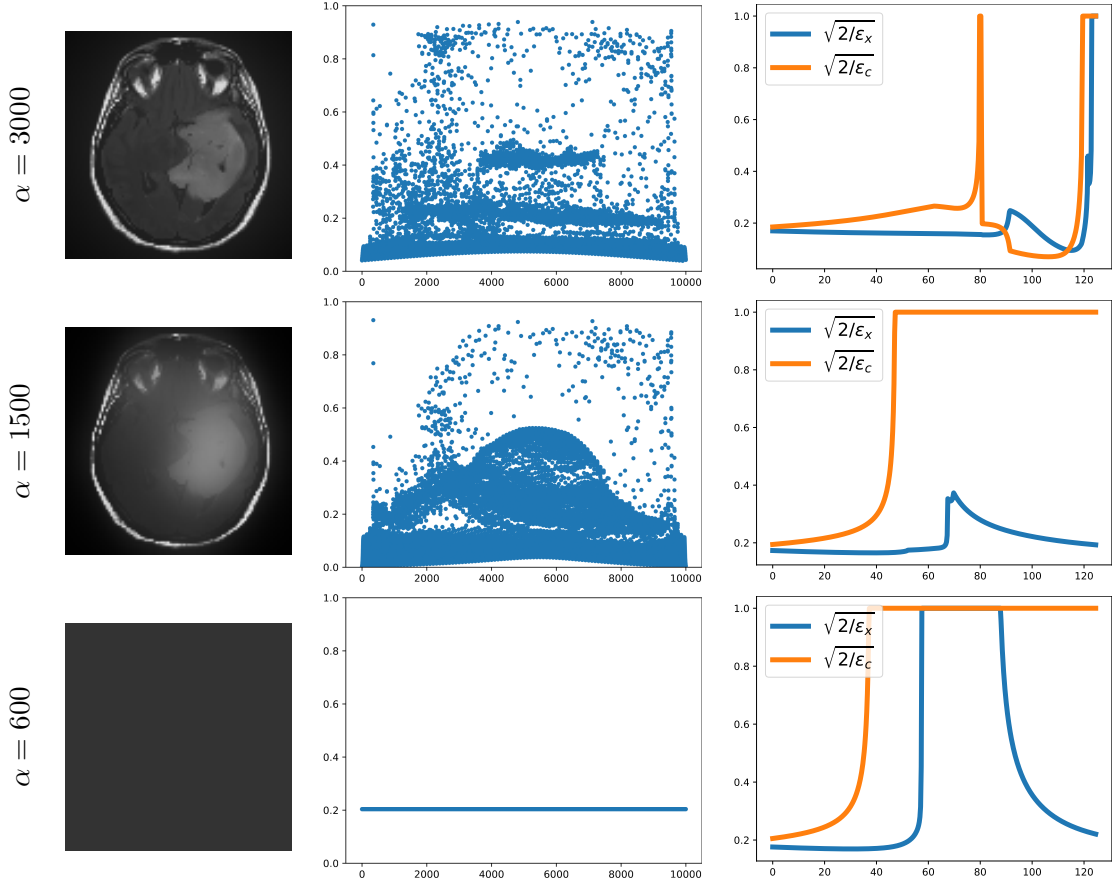


Figure 2: Output of Algorithm 1 for different values of the fidelity parameter α , using the image in Figure 1 as input. On each row, from left to right: output image, grey level for every pixel, time evolution of the semi-axes of the ellipsoid (2).

- $\mu \mapsto \int_{\Omega} \mu \cdot (v - \nabla u)$ is linear, therefore concave.

Finally, as in the proof of Theorem 3.1, it is immediate to show coercivity in the primal variables, ensuring that the minimum is attained in a weakly compact set. The ensemble of these properties is sufficient to guarantee the existence of a saddle point in our setting (see for instance [16, Chapter VI]) and strong duality is directly implied by it. \square

In general, the saddle point is not unique. In fact, when approaching the minimum point (u^*, v^*) in the primal variables (which is unique), the term $\int_{\Omega} \mu \cdot (v^* - \nabla u^*)$ vanishes, so that any $\mu \in L^2(\Omega; \mathbb{R}^2)$ becomes feasible. However, this does not pose an issue for the numerical algorithms, which will converge to the unique primal solution and to one of the optimal dual ones.

In conclusion, we consider (13) in our image processing framework and state the following optimal control problem:

$$\underset{\varepsilon \in \mathcal{E}, v \in L^2(\Omega; \mathbb{R}^2)}{\text{minimise}} \quad \underset{\mu \in L^2(\Omega; \mathbb{R}^2)}{\text{maximise}} \quad L(c(\cdot, T; \varepsilon), v, \mu) \quad \text{subject to (1)-(2).} \quad (15)$$

4.1 Numerical approximation

To solve the saddle point problem (15), we adopt an iterative approximation scheme, called the Alternating Direction Method of Multipliers (ADMM) [4]. It essentially consists in optimising one variable at a time, keeping the other two fixed. As already highlighted in Section 3.1, we

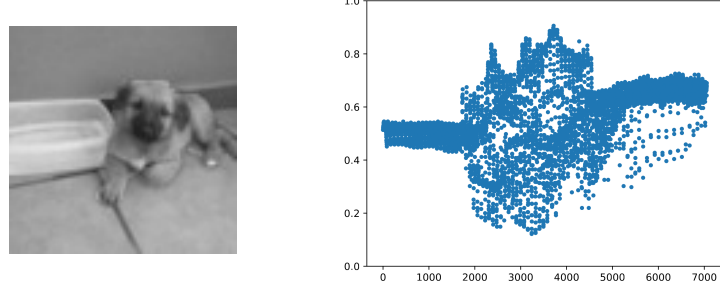


Figure 3: Portrait of baby Namou, S. Cacace's dog. On the left side, the original picture; on the right, colour value $c_i \in [0, 1]$ for every pixel p_i , $i = 1, \dots, N$.

lose convexity in the control-to-state map $\varepsilon \mapsto c(\cdot, T; \varepsilon)$, so we can only expect convergence to a local minimum in the first variable.

The key observation for ADMM is that, for any fixed μ , the cost functional L presents the same minimisers of

$$\begin{aligned} \tilde{L}(u, v) &:= \int_{\Omega} \frac{\rho}{2} \left| v(x) - \nabla u(x) + \frac{\mu(x)}{\rho} \right|^2 + |v(x)| + \frac{\alpha}{2} (u(x) - I(x))^2 \, dx \\ &= L(u, v, \mu) + \int_{\Omega} \frac{|\mu(x)|^2}{2\rho} \, dx. \end{aligned} \quad (16)$$

As a consequence, for the minimisation in the u variable we can adapt Algorithm 1, substituting the final cost J in the augmented Lagrangian formulation with the new \tilde{L} , assuming for the moment that v is also fixed. With this procedure, we get to an optimality system that is the same as (7), except for equation (7b). As a matter of fact, we now have

$$\tilde{L}'(u)[w] = \int_{\Omega} [\operatorname{div}(\mu + \rho v - \rho \nabla u) + \alpha(u - I)] \cdot w,$$

therefore the terminal condition for the adjoint state λ becomes

$$\lambda(x, T) = -\rho \Delta u(x) + \operatorname{div}(\mu(x) + \rho v(x)) + \alpha(u(x) - I(x)), \quad x \in \Omega. \quad (17)$$

It is worth noticing that for $0 < \rho \ll 1$ the Laplacian term can become arbitrarily small. This means that now, by tuning the parameter ρ , we can mitigate diffusion, which is the cause of the blur effect in the tests presented in Section 3.2.

For the minimisation in the v variable, we observe that v^* is a minimiser of $\tilde{L}(u, \cdot)$ if and only if it minimises point-wise the non negative integrand $v \mapsto \frac{\rho}{2}|v - \nabla u + \frac{\mu}{\rho}|^2 + |v|$. To keep the notation compact, consider the function $f(v) = \frac{\rho}{2}|v - a|^2 + |v|$, where a is fixed. Then, if $|a| \leq \frac{1}{\rho}$,

$$\begin{aligned} f(v) &= \frac{\rho}{2}|v|^2 + \frac{\rho}{2}|a|^2 - \rho v \cdot a + |v| \\ &\geq \frac{\rho}{2}|v|^2 + \frac{\rho}{2}|a|^2 - \rho|v||a| + |v| \\ &\geq \frac{\rho}{2}|a|^2 + (1 - \rho|a|)|v| \geq \frac{\rho}{2}|a|^2 = f(0), \end{aligned}$$

for all v , meaning $v^* = 0$. Conversely, if $|a| > \frac{1}{\rho}$, since f is convex, for any $v \neq 0$ we can impose

$$f'(v) = \rho(v - a) + \frac{v}{|v|} = 0. \quad (18)$$

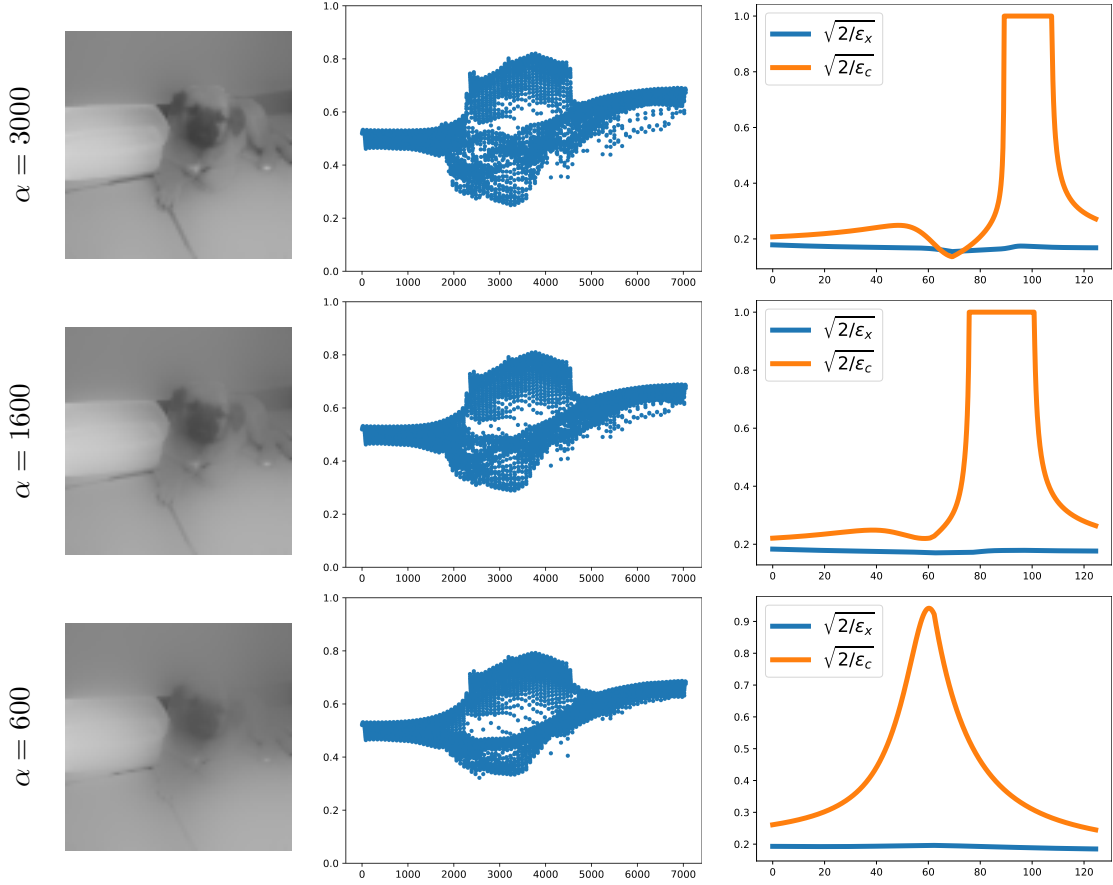


Figure 4: Output of Algorithm 1 for different values of the fidelity parameter α , using the image in Figure 3 as input. On each row, from left to right: output image, grey level for every pixel, time evolution of the semi-axes of the ellipsoid (2).

Moreover, in order to minimise f , it must be $v^* = c \frac{a}{|a|}$, for some $c > 0$. By plugging this expression into (18), we get

$$\rho \left(c \frac{a}{|a|} - a \right) + \frac{a}{|a|} = 0,$$

which yields $c = |a| - \frac{1}{\rho}$. Going back to the original problem, we obtain an explicit minimisation in the v variable, the so-called shrinkage formula [4, 15]:

$$\operatorname{argmin}_v L(u, v, \mu) = \operatorname{argmin}_v \tilde{L}(u, v) = \begin{cases} 0 & \text{if } |a| \leq \frac{1}{\rho}, \\ \left(|a| - \frac{1}{\rho} \right) \frac{a}{|a|} & \text{otherwise,} \end{cases} \quad (19)$$

where $a = \nabla u - \frac{\mu}{\rho}$.

Finally, for the maximisation in the dual variable μ , it is enough to perform a simple gradient ascent in the direction $v - \nabla u$, since the cost functional L is linear in μ .

The ADMM algorithm alternates a partial optimisation in each individual variable u, v, μ , performed as outlined above, until a maximum number of iterations is reached, or until the gap between the subsequent decrease and increase in the cost functional – given, respectively, by the minimisation in the primal variables and the maximisation in the dual one – is small enough. This is the reason why Theorem 4.1 is fundamental: it ensures that there is no duality gap. We also remark that, thanks to (19), despite introducing two additional variables, the overall cost is that of just two nested loops, not three. The detailed routine is reported in Algorithm 2.

Algorithm 2 ADMM algorithm for the saddle point problem (15)

Require: Initial guesses for the control $\varepsilon^{(0)}$ and the dual variable $\mu^{(0)}$, $\gamma > 0$

- 1: Integrate (7a) forward in time to obtain $c^{(0)}$
- 2: Compute $v^{(0)}$ using (19)
- 3: $j \leftarrow 1$
- 4: **repeat**
- 5: Compute $\varepsilon^{(j)}$ and $c^{(j)}$ using Algorithm 1 modified with (17)
- 6: Compute $v^{(j)}$ using (19)
- 7: $\mu^{(j+1)} \leftarrow \mu^{(j)} + \gamma (v^{(j)} - \nabla c^{(j)}(\cdot, T))$
- 8: $j \leftarrow j + 1$
- 9: **until** stop criterion is verified

Remark 3. The two-way line search utilised in Algorithm 1 can also be employed to select a dynamic ascent step-size $\gamma^{(j)}$, on line 7 of Algorithm 2. We illustrated the process with a fixed step length for simplicity.

4.2 Numerical tests

In this section, we report a comparison between the outputs of Algorithm 1 and Algorithm 2 on the same test images used in Section 3.2. Additionally, we perform a third test on a more complex image. The discretisations and parameters used for the ADMM are exactly the same of Section 3.2, as well as the interaction kernel. The regularisation parameter is set to $\rho = 10^{-2}$ and the ascent step size is $\gamma = 10^{-2}$. Algorithm 2 was also implemented in CUDA C and run on the same GPU as before.

The first test is carried out on the MRI scan in Figure 1, on which Algorithm 1 works best. The results are shown in Figure 5. Despite finding qualitatively similar controls, reported on the bottom row, the healthy brain tissue and the tumour are depicted as more uniform clusters by Algorithm 2, without detailing them excessively, and at the same time without any blurring.

Figure 6 illustrates the comparison using the dog picture in Figure 3. In this case, it is evident how Algorithm 2 mitigates diffusion, unlike Algorithm 1, which tends to blur the image as already mentioned. Not only do the edges appear sharper in the top-right picture, but the segments themselves are more even. This can be verified also by looking at the colour distributions in the middle row: the clusters created by Algorithm 2 are more concentrated and fewer pixels exhibit an intermediate colour.

To conclude, we perform a final experiment on an image that presents mixed features. Looking at the original picture on the top-left of Figure 7, we notice both large areas with high contrast (the floor, the irregular wall on the right, the dark plants in the background) and a central subject with many details and shades of grey. The output of Algorithm 1 is definitely unsatisfactory. Even if the larger areas are smoothed out, the diffusion effect due to global interactions in the colour component (see the bottom-centre plot in Figure 7) is dominant. As a consequence, not even the white wall is homogenised correctly and the railing in the background is almost fused with the trees. Overall, Algorithm 1 acts more like a denoiser in this test. On the contrary, Algorithm 2 preserves all the edges neatly, even enhancing the contrast in some areas. The floor and the wall on the side are evened out, and the dog is perfectly outlined. The difference between the two outputs can be seen in the colour distribution as well. While there are almost no clusters in the one given by Algorithm 1, we can clearly identify them in the middle-right plot. Indeed, the optimal controls found by the two algorithms are completely different, as can be seen on the bottom row of Figure 7.

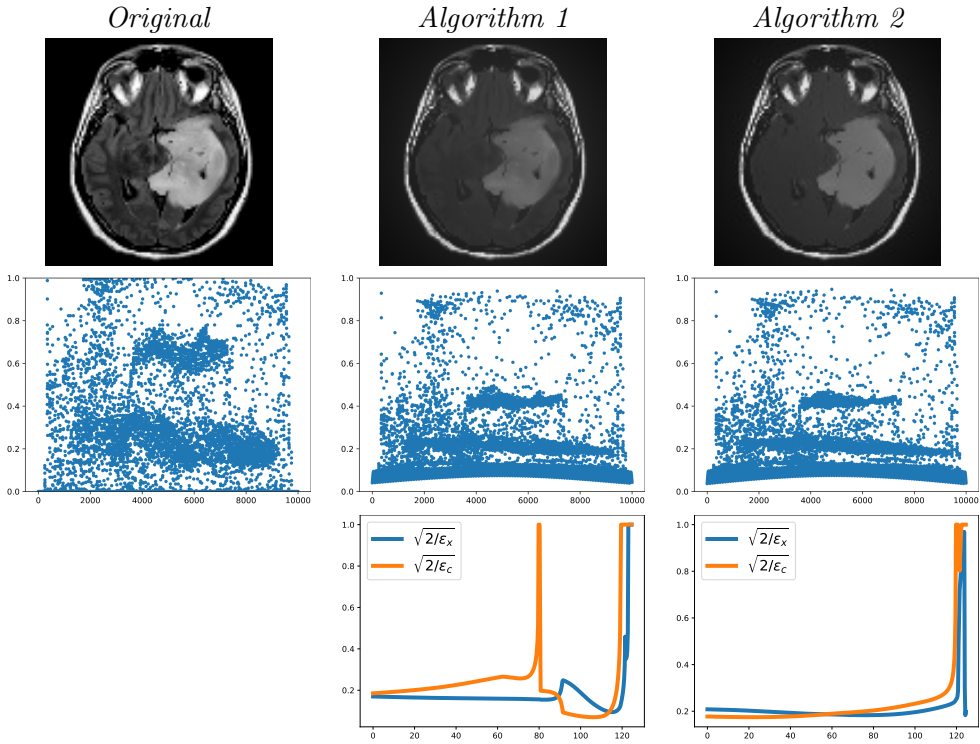


Figure 5: Comparison of Algorithm 1 and Algorithm 2 on the test image in Figure 1. Output image on top, grey level for every pixel in the middle row, time evolution of the semi-axes of the ellipsoid (2) on the bottom.

5 Conclusions and perspectives

In this paper, we introduced a novel approach for image quantization and segmentation by framing them as an optimal control problem for a multi-agent system. The core idea is to control the colour dynamics of image pixels to form clusters that correspond to different segments of the image. This is achieved by defining a cost functional that balances colour variation and fidelity to the original image. Initially, a model based on a quadratic cost functional for the colour gradient was proposed and the optimisation problem was solved using a direct–adjoint looping (DAL) algorithm. Numerical experiments demonstrated that this approach is effective for images with high-contrast features, such as medical MRI scans. However, it was found to produce a blurring effect and was less suitable for natural images with smoother colour transitions, where it acted more like a denoising filter. To address these limitations, a more sophisticated model incorporating total variation was introduced. This model is based on the Rudin-Osher-Fatemi (ROF) functional, which is well-suited for preserving sharp edges. Due to the non-differentiability of the total variation term, the minimisation problem was regularised and reformulated as a saddle-point problem, which was solved numerically using the Alternating Direction Method of Multipliers (ADMM). This primal-dual approach effectively mitigates the diffusion and blurring effects observed with the first model. Comparative numerical tests on various images showcased the superior performance of the ADMM-based total variation model. It successfully segmented images with both high-contrast and complex, detailed regions, preserving sharp edges and creating more uniform colour clusters. The parallel implementation of the numerical schemes on a GPU using CUDA significantly improved computational performance, highlighting the potential of this methodology for handling high-dimensional data.

Future work could involve a comparison with other state-of-the-art segmentation tools, as well as explore the application of this framework to colour images. Further research could also investigate the mean-field limit of the model or introduce stochastic methods, in order to treat

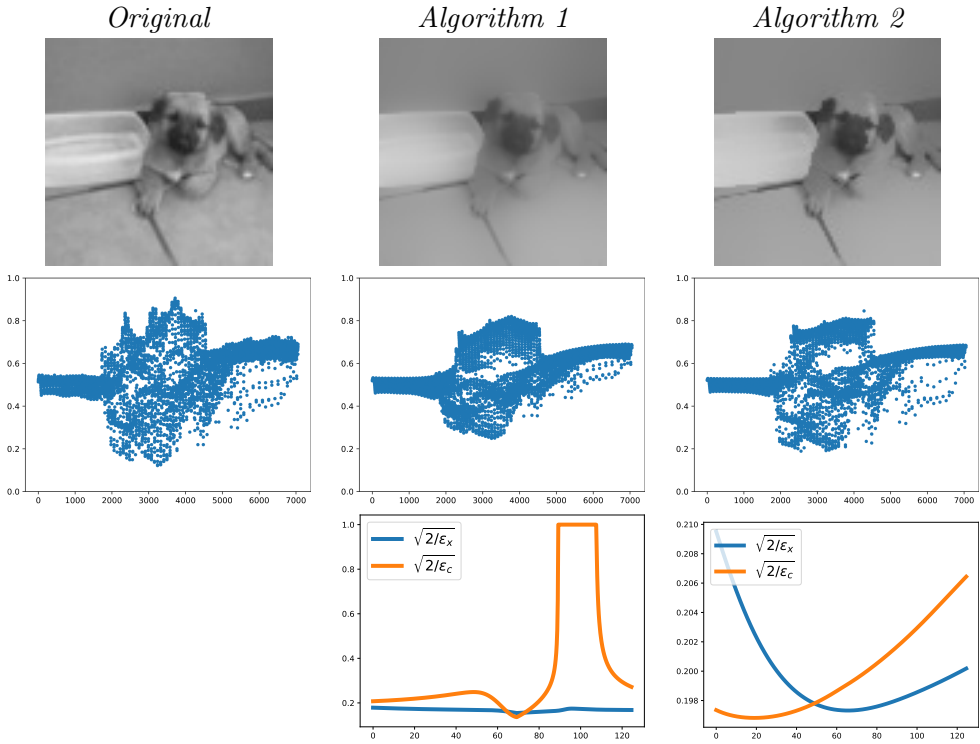


Figure 6: Comparison of Algorithm 1 and Algorithm 2 on the test image in Figure 3. Output image on top, grey level for every pixel in the middle row, time evolution of the semi-axes of the ellipsoid (2) on the bottom.

high-resolution images more efficiently.

Acknowledgments

We declare that no dog was harmed for the execution of the numerical tests.

This work was supported by the Italian National Group of Scientific Computing (GNCS-INDAM). The authors also acknowledge the support of Sapienza University of Rome for the project “Advanced Computational Methods for Real-World Applications: Data-Driven Models, Hyperbolic Equations and Optimal Control”, CUP: B83C25000880005.

A.O. is supported by the European Union – Next Generation EU, Mission 4, Component 1, CUP 351: B83C22003530006.

S.C. is supported by the PNRR-MUR project “Italian Research Center on High Performance Computing, Big Data and Quantum Computing”.

G.V. acknowledges the support of MUR (Ministry of University and Research) under the MUR-PRIN PNRR Project 2022 No. P2022JC95T “Data-driven discovery and control of multi-scale interacting artificial agent system”.

References

- [1] G. Albi, L. Pareschi, G. Toscani, and M. Zanella. Recent advances in opinion modeling: Control and social influence. In M. Burger and J. D. Goddard, editors, *Active Particles, Vol. 1, Modeling, Simulation, Science and Technology*, pages 49–98. Birkhäuser/Springer, Cham, Switzerland, 2017.

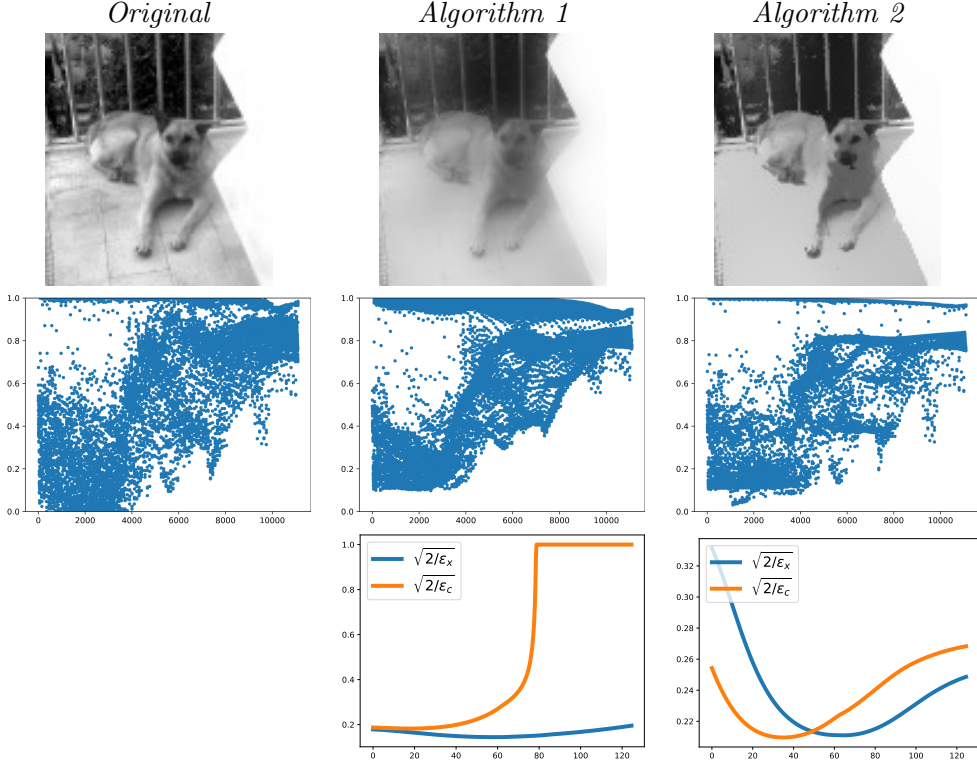


Figure 7: Comparison of Algorithm 1 and Algorithm 2 on another test image potraying adult Namou. Output image on top, grey level for every pixel in the middle row, time evolution of the semi-axes of the ellipsoid (2) on the bottom.

- [2] P. Arbeláez, M. Maire, C. Fowlkes, and J. Malik. Contour detection and hierarchical image segmentation. *IEEE Transactions on Pattern Analysis and Machine Intelligence*, 33(5):898–916, 2011.
- [3] L. Armijo. Minimization of functions having Lipschitz continuous first partial derivatives. *Pacific Journal of mathematics*, 16(1):1–3, 1966.
- [4] S. Boyd, N. Parikh, E. Chu, B. Peleato, J. Eckstein, et al. Distributed optimization and statistical learning via the alternating direction method of multipliers. *Foundations and Trends® in Machine learning*, 3(1):1–122, 2011.
- [5] R. F. Cabini, A. Pichieccio, A. Lascialfari, S. Figini, and M. Zanella. A kinetic approach to consensus-based segmentation of biomedical images. *Kinetic and Related Models*, 18(2):286–311, 2025.
- [6] S. Cacace and A. Oliviero. Reliable optimal controls for SEIR models in epidemiology. *Mathematics and Computers in Simulation*, 223:523–542, 2024.
- [7] A. Chambolle and P.-L. Lions. Image recovery via total variation minimization and related problems. *Numerische Mathematik*, 76(2):167–188, 1997.
- [8] A. Chambolle and T. Pock. A first-order primal-dual algorithm for convex problems with applications to imaging. *Journal of mathematical imaging and vision*, 40(1):120–145, 2011.
- [9] L.-C. Chen, G. Papandreou, I. Kokkinos, K. Murphy, and A. L. Yuille. Deeplab: Semantic image segmentation with deep convolutional nets, atrous convolution, and fully connected crfs. In *IEEE Transactions on Pattern Analysis and Machine Intelligence*, volume 40, pages 834–848, 2018.

- [10] H.-D. Cheng, X. H. Jiang, Y. Sun, and J. Wang. Color image segmentation: advances and prospects. *Pattern Recognition*, 34(12):2259–2281, 2001.
- [11] F. Clarke. *Functional analysis, calculus of variations and optimal control*. Springer, 2013.
- [12] D. Comaniciu and P. Meer. Mean shift: A robust approach toward feature space analysis. *IEEE Transactions on Pattern Analysis and Machine Intelligence*, 24(5):603–619, 2002.
- [13] F. Cucker and S. Smale. Emergent behavior in flocks. *IEEE Transactions on Automatic Control*, 52(5):852–862, 2007.
- [14] W. Dehnen and H. Aly. Improving convergence in smoothed particle hydrodynamics simulations without pairing instability. *Monthly Notices of the Royal Astronomical Society*, 425(2):1068–1082, 2012.
- [15] D. L. Donoho and I. M. Johnstone. Ideal spatial adaptation by wavelet shrinkage. *Biometrika*, 81(3):425–455, 1994.
- [16] I. Ekeland and R. Temam. *Convex analysis and variational problems*. Society for Industrial and Applied Mathematics, 1999.
- [17] X. Gong, M. Herty, B. Piccoli, and G. Visconti. Crowd dynamics: Modeling and control of multiagent systems. *Annual Review of Control, Robotics, and Autonomous Systems*, 6:261–282, 2023.
- [18] J. Han, C. Yang, X. Zhou, and W. Gui. A new multi-threshold image segmentation approach using state transition algorithm. *Applied Mathematical Modelling*, 44:588–601, 2017.
- [19] R. Hegselmann and U. Krause. Opinion dynamics and bounded confidence: Models, analysis and simulation. *Journal of Artificial Societies and Social Simulation*, 5(3), 2002.
- [20] M. Herty, L. Pareschi, and G. Visconti. Mean field models for large data–clustering problems. *Networks and Heterogeneous Media*, 15(3):463–487, 2020.
- [21] M. H. Hesamian, W. Jia, X. He, and P. Kennedy. Deep learning techniques for medical image segmentation: Achievements and challenges. *Journal of Digital Imaging*, 32(4):582–596, 2019.
- [22] X. Liu, Y. Qiao, X. Chen, J. Miao, and L. Duan. Color image segmentation based on modified Kuramoto model. *Procedia Computer Science*, 88:245–258, 2016.
- [23] X. Liu, L. Song, S. Liu, and Y. Zhang. A review of deep-learning-based medical image segmentation methods. *Sustainability*, 13(3):1224, 2021.
- [24] M. Martucci, R. Russo, F. Schimperna, G. D’Apolito, M. Panfili, A. Grimaldi, A. Perna, A. M. Ferranti, G. Varcasia, C. Giordano, and S. Gaudino. Magnetic resonance imaging of primary adult brain tumors: State of the art and future perspectives. *Biomedicines*, 11(2), 2023.
- [25] H. Mittal, A. C. Pandey, M. Saraswat, S. Kumar, R. Pal, and G. Modwel. A comprehensive survey of image segmentation: Clustering methods, performance parameters, and benchmark datasets. *Multimedia Tools and Applications*, pages 1–26, 2021.
- [26] S. Motsch and E. Tadmor. Heterophilious dynamics enhances consensus. *SIAM Review*, 56(4):577–621, 2014.
- [27] L. S. Pontryagin, V. G. Boltyanskii, R. V. Gamkrelidze, and E. F. Mishchenko. *The Mathematical Theory of Optimal Processes*. Interscience Publishers, New York, 1962.

- [28] O. Ronneberger, P. Fischer, and T. Brox. U-net: Convolutional networks for biomedical image segmentation. In *Proceedings of the International Conference on Medical Image Computing and Computer-Assisted Intervention (MICCAI)*, volume 9351 of *Lecture Notes in Computer Science*, pages 234–241. Springer, 2015.
- [29] L. I. Rudin, S. Osher, and E. Fatemi. Nonlinear total variation based noise removal algorithms. *Physica D: nonlinear phenomena*, 60(1-4):259–268, 1992.
- [30] P. Shan. Image segmentation method based on K-mean algorithm. *EURASIP Journal on Image and Video Processing*, 2018:81, 2018.
- [31] N. Sharma and L. M. Aggarwal. Automated medical image segmentation techniques. *Journal of Medical Physics*, 35(1):3–14, 2010.
- [32] F. Tröltzsch. *Optimal control of partial differential equations: theory, methods and applications*. American Mathematical Society, 2024.
- [33] H. Wendland. Piecewise polynomial, positive definite and compactly supported radial functions of minimal degree. *Advances in computational Mathematics*, 4(1):389–396, 1995.
- [34] Z. Yu, O. C. Au, R. Zou, W. Yu, and J. Tian. An adaptive unsupervised approach toward pixel clustering and color image segmentation. *Pattern Recognition*, 43(5):1889–1906, 2010.

A Derivation of the optimality system (7)

We describe here the explicit formal derivation of the first order optimality system (7), starting from the cost functional (6), which we report for ease of reading

$$\tilde{J}(c, \lambda, \varepsilon) = \int_0^T \int_{\Omega} \lambda(x, t) \cdot [\partial_t c(x, t) - F(c(x, t), \varepsilon(t))] \, dx dt + \int_{\Omega} \frac{1}{2} |\nabla c(x, T)|^2 + \frac{\alpha}{2} (c(x, T) - I(x))^2 \, dx.$$

When it does not create ambiguity, we will omit the dependencies on x and t to keep the notation as simple as possible. We will also assume that all the functions are of class C^2 .

First, we compute the variation with respect to c in the direction v . Since any admissible perturbation must preserve the initial data of system (1), we impose $v(x, 0) = 0$. Moreover, we set zero homogeneous Neumann boundary conditions on $\partial\Omega$. This choice is the most natural in image processing, as it does not create any artifacts on the border of the image. A Dirichlet condition, for example, would prescribe a predefined colour on $\partial\Omega$, which would artificially increase the cost.

$$\begin{aligned} \tilde{J}'(c)[v] &= \int_0^T \int_{\Omega} \lambda \cdot [\partial_t v - \partial_c F(c, \varepsilon) \cdot v] \, dx dt + \int_{\Omega} \nabla c(x, T) \cdot \nabla v(x, T) + \alpha(c(x, T) - I) v(x, T) \, dx \\ &= \int_{\Omega} \lambda(x, T) v(x, T) \, dx - \int_{\Omega} \int_0^T [-\partial_t \lambda - \partial_c F(c, \varepsilon) \cdot \lambda] v \, dt dx + \\ &\quad + \int_{\Omega} [-\Delta c(x, T) + \alpha(c(x, T) - I)] v(x, T) \, dx, \end{aligned}$$

where we used integration by parts and the divergence theorem. Now, imposing $\tilde{J}'(c)[v] = 0$ for any direction v , by the Fundamental Lemma of the calculus of variations we get equation (7b), that is for a.e. $(x, t) \in \Omega \times (0, T)$

$$\begin{aligned} \partial_t \lambda(x, t) &= -\partial_c F(c(x, t), \varepsilon(t)) \cdot \lambda(x, t), \\ \lambda(x, T) &= -\Delta c(x, T) + \alpha(c(x, T) - I(x)). \end{aligned}$$

Equation (7a), i.e. the dynamics, is immediately derived by observing that \tilde{J} is linear in the adjoint variable λ , therefore $\tilde{J}'(\lambda)[w] = 0$ for all w if and only if $\partial_t c(x, t) = F(c(x, t), \varepsilon(t))$, with the natural initial condition $c(x, 0) = I(x)$.

Finally, we proceed analogously with the variation with respect to ε , which explicitly appears only in the first term:

$$\tilde{J}'(\varepsilon)[z] = \int_0^T \int_{\Omega} -\lambda(x, t) \cdot \partial_{\varepsilon} F(c(x, t), \varepsilon(t)) dx z(t) dt = 0$$

if and only if

$$\int_{\Omega} \lambda(x, t) \cdot \partial_{\varepsilon} F(c(x, t), \varepsilon(t)) dx = 0 \quad \text{for a.e. } t \in (0, T). \quad (7c)$$

Note that in the numerical approximation we do not solve (7c) directly, but rather we use the discrete functional gradient

$$\partial_{\varepsilon}^{\#} \tilde{J}(\varepsilon(t)) = \begin{bmatrix} \sum_i \lambda_i(t) \partial_{\varepsilon_x} F(c_i(t), \varepsilon(t)) \\ \sum_i \lambda_i(t) \partial_{\varepsilon_c} F(c_i(t), \varepsilon(t)) \end{bmatrix}$$

to perform the control update in Algorithm 1.